

This item is likely protected under Title 17 of the U.S. Copyright Law. Unless on a Creative Commons license, for uses protected by Copyright Law, contact the copyright holder or the author.

Access to this work was provided by the University of Maryland, Baltimore County (UMBC) ScholarWorks@UMBC digital repository on the Maryland Shared Open Access (MD-SOAR) platform.

**Please provide feedback**

Please support the ScholarWorks@UMBC repository by emailing [scholarworks-group@umbc.edu](mailto:scholarworks-group@umbc.edu) and telling us what having access to this work means to you and why it's important to you. Thank you.

# MULTIWAVELENGTH OBSERVATIONS OF THE GALACTIC BLACK HOLE TRANSIENT 4U 1543–47 DURING OUTBURST DECAY: STATE TRANSITIONS AND JET CONTRIBUTION

E. KALEMCI,<sup>1</sup> J. A. TOMSICK,<sup>2</sup> M. M. BUXTON,<sup>3</sup> R. E. ROTHSCHILD,<sup>2</sup> K. POTTSCHMIDT,<sup>4,5</sup>  
 S. CORBEL,<sup>6</sup> C. BROCKSOPP,<sup>7</sup> AND P. KAARET<sup>8</sup>

*Received 2004 September 3; accepted 2004 November 24*

## ABSTRACT

Multiwavelength observations of Galactic black hole (GBH) transients during state transitions and in the low/hard state may provide detailed information on the accretion structure of these systems. The object 4U 1543–47 is a GBH transient that was covered exceptionally well in X-rays and the infrared (daily observations) and reasonably well in the optical and radio during its outburst decay in 2002. When all the available information is gathered from the intermediate and the low/hard states, 4U 1543–47 makes an important contribution to our understanding of state transitions and the role of outflows in the high-energy emission properties of black hole binaries. The evolution of the X-ray spectral and temporal properties and the infrared light curve place strong constraints on different models to explain the overall emission from accreting black holes. The overall spectral energy distribution is consistent with a synchrotron origin for the optical and infrared emission; however, the X-ray flux is above the power-law continuation of the optical and infrared flux. The infrared light curve, the HEXTE light curve, and the evolution of the X-ray photon index indicate that the major source of hard X-rays cannot be direct synchrotron radiation from an acceleration region in a jet for most of the outburst decay.

*Subject headings:* accretion, accretion disks — binaries: close — black hole physics — stars: individual (4U 1543–47) — X-rays: binaries

## 1. INTRODUCTION

Galactic black hole (GBH) transients are binary systems that can show orders-of-magnitude increases in luminosity during outbursts caused by sudden, dramatic increases of mass accretion onto compact objects. During an outburst, a GBH transient often follows a specific sequence of X-ray spectral states; it is in the “hard” or “low/hard” (LH) state at the beginning and also during the decay of an outburst. Between the rise and the decay, when the 2–10 keV luminosity is high, the system is usually in the “thermal-dominant” (TD) state (historically this was called the high/soft state), and sometimes in the “steep power-law” state (historically, the very high state; see McClintock & Remillard 2003 for a detailed discussion of spectral states). They can also be found in an intermediate state (IS), where source characteristics do not fit into the TD or LH state but show various combinations of these states, especially close to state transitions (McClintock & Remillard 2003). The sequence of spectral states may be complicated, or it may be very simple, as some sources stay in the LH state throughout their outbursts (Kalemci 2002; Brocksopp et al. 2004; references therein). However, the systems are almost always found in the LH state during outburst decay (Kalemci

2002), before they return to quiescence (perhaps a continuation of the LH state at very low luminosities; Corbel et al. 2000; Kong et al. 2002; Tomsick et al. 2004).

In terms of timing, the TD state is characterized by a lack or very low level of variability (a few percent rms between 0.04 and 4 Hz), whereas the LH state shows strong variability ( $\sim 30\%$  rms in the same band) along with quasi-periodic oscillations (QPOs) in the power density spectrum. Other Fourier analysis-related timing tools, such as “coherence” and “lag” behavior, are also different in each state (see Vaughan & Nowak 1997 and Nowak et al. 1999 for detailed definitions of these quantities). The mean coherence is very high ( $\sim 1$ ) in the LH state, and the mean lag is either zero or very low between the 3–6 keV and 6–15 keV bands in the 1–10 Hz frequency range. During the IS and during transitions, however, the coherence is lower and the lag is higher in the same frequency band and between the same energy bands (Pottschmidt et al. 2000; Kalemci 2002).

The relation between the radio emission and the X-ray states has been well established (McClintock & Remillard 2003; see also Corbel et al. 2004 and the recent review by Fender [2005]). In the TD state, the radio emission is often quenched (Fender et al. 1999; Corbel et al. 2000). Optically thin outflows are sometimes detected during state transitions (Fender & Kuulkers 2001; Corbel et al. 2001), and powerful, compact jets are always observed in the LH state (Fender 2001). In addition, there exists a global correlation between the X-ray flux and the radio flux for different sources at different luminosities in the LH state (Corbel et al. 2003; Gallo et al. 2003). The base of the jet might provide the energetic electrons that would create the X-ray power law in the spectrum, establishing the link between the radio and the X-ray flux (Fender 2001). The fact that the lags are higher during state transitions, when the optically thin, large outflows are observed, may also point to a relation between the radio jet and energetic electrons (Pottschmidt et al. 2000; Kalemci et al. 2003). An alternative model is that the X-ray emission is synchrotron in

<sup>1</sup> Space Sciences Laboratory, 7 Gauss Way, University of California at Berkeley, Berkeley, CA 94720-7450.

<sup>2</sup> Center for Astrophysics and Space Sciences, University of California, San Diego, 9500 Gilman Drive, La Jolla, CA 92093-0424.

<sup>3</sup> Department of Astronomy, Yale University, New Haven, CT 06511-8101.

<sup>4</sup> Max-Planck-Institut für Extraterrestrische Physik, Giessenbachstrasse 1, D-85748 Garching, Germany.

<sup>5</sup> INTEGRAL Science Data Centre, Chemin d’Ecogia 16, CH-1290 Versoix, Switzerland.

<sup>6</sup> Université Paris VII and Service d’Astrophysique, CEA Saclay, F-91191 Gif-sur-Yvette, France.

<sup>7</sup> Mullard Space Science Laboratory, Holmbury St. Mary, Dorking, Surrey RH5 6NT, UK.

<sup>8</sup> Department of Physics and Astronomy, University of Iowa, Iowa City, IA 52242-1479.

nature and comes directly from a shock region in the jet (Falcke & Biermann 1999; Markoff et al. 2001). This model can explain the radio–X-ray flux correlation naturally; however, it fails to make any predictions about the details of the X-ray spectrum.<sup>9</sup>

The daily observations of transients in the optical and the infrared by the YALO consortium (Bailyn et al. 1999) provide another dimension in the study of GBH transients. A secondary maximum in the *V*, *B*, *I*, *J*, and *K* bands has been observed during the outburst decay of 4U 1543–47 (Buxton & Bailyn 2004). A similar secondary maximum was also observed in the *V*, *I*, and *H* bands during the outburst decay of XTE J1550–564 in 2000 (Jain et al. 2001a). The properties of the optical emission during the secondary maximum of the 2000 outburst of XTE J1550–564 indicate a synchrotron origin from a jet (Corbel et al. 2001), rather than X-ray reprocessing at the outer parts of the accretion disk, which was suggested to explain the optical light curves of the same source in its 1998 outburst (and also other GBH transients; Jain et al. 2001a, 2001b). X-ray reprocessing as the origin of optical emission has also been questioned by Brocksopp et al. (2004) because of a lack of correlation between the X-ray and optical light curves of V404 Cyg, GRO J1719–24, GRO J0422+32, GS 1354–64, and XTE J1118+480. The observations of GX 339–4 in the optical and the near-infrared (NIR) in the LH state show a nonthermal, optically thin synchrotron component that can be extrapolated down to the X-ray spectrum (Corbel & Fender 2002). A very recent study of GX 339–4 with good optical, infrared, and X-ray monitoring points out that in the LH state, the NIR emission has a synchrotron origin in a jet; however, the source of the optical emission may be a combination of a jet, the disk, and possibly a compact corona in this source (Homan et al. 2005). In addition, the LH state during the rise of the 2002 outburst of GX 339–4 showed a strong correlation between X-ray flux and optical/NIR, similar to the radio–X-ray flux correlation (Homan et al. 2005).

One of the most interesting epochs of an outburst is its decay, because it is almost guaranteed that there will be a transition to the LH state that provides additional information about the system through various timing-analysis techniques, and also through strong radio emission. Analysis of state transitions helps us probe the accretion dynamics of these systems. Our group has been observing GBH transients during outburst decays in X-rays with the *Rossini X-Ray Timing Explorer* (*RXTE*) and in radio to understand the evolution before, during, and after the transition to the LH state (Kalemci et al. 2001; Tomsick et al. 2001; Kalemci et al. 2003; Tomsick et al. 2003). A uniform analysis of all GBH transients observed with approximately daily coverage with *RXTE* between 1996 and 2001 resulted in a better understanding of the evolution of spectral and temporal parameters during the outburst decay (Kalemci et al. 2004). The most striking of all the results is that the sharpest change indicating a state transition is observed in the timing properties (usually a jump in the rms amplitude of variability from less than a few percent to tens of percent in less than a day). This change in the rms amplitude is often (but not always) accompanied by a sharp increase in the power-law flux. Such sharp changes in the rms amplitude of variability were noted as the times of state transition in Kalemci et al. (2004), and the same convention is applied here.

In this work, we will try to obtain a coherent picture of changes in the physical properties of a GBH transient, 4U 1543–47,

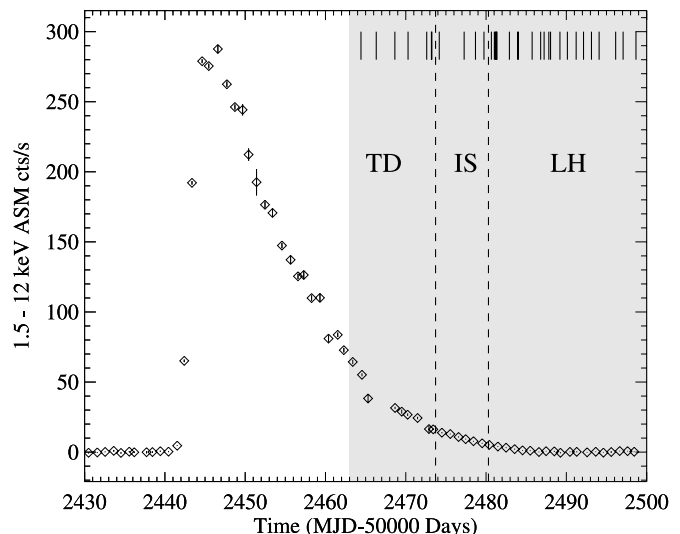


FIG. 1.—The 1.5–12 keV ASM light curve of the 2002 outburst of 4U 1543–47. We worked on the decay part of the outburst and analyzed *RXTE* data shown in the gray region. The vertical bars indicate pointed PCA observations. The dashed lines indicate approximate times of state transitions.

around state transitions and also deep in the LH state, using multiwavelength observations. This object was discovered by the *Uhuru* satellite on 1971 August 17 (Matilsky et al. 1972). The source was observed again in outburst in 1983, in 1992, and also in 2002 (Kitamoto et al. 1984; Harmon et al. 1992; Miller & Remillard 2002; Brocksopp et al. 2004). The optical counterpart was found by Pedersen (1983). Initial dynamical mass measurements during quiescence established this source as a black hole binary system with a compact-object mass between  $2.7$  and  $7.5 M_{\odot}$  (Orosz et al. 1998). A more accurate value of  $9.4 \pm 2.0 M_{\odot}$  is given by Park et al. (2004) based on a work in preparation by J. Orosz. The 2002 outburst was first detected by the All-Sky Monitor (ASM) on *RXTE* on MJD 52,442 (Miller & Remillard 2002; Park et al. 2004). Around a month later, as the outburst was decaying, our group started its daily monitoring campaign with *RXTE* and caught the transition to a harder state on MJD 52,479 (Kalemci et al. 2002), although subsequent analysis in this work indicates that the transition started earlier. An analysis of the *RXTE* data before the LH state, with an emphasis on broad iron reflection lines, is given by Park et al. (2004). Figure 1 shows the ASM light curve of the overall outburst, the epoch we analyzed, and the dates of pointed observations used in this work. The source was also detected and observed in the radio and optical bands (see Park et al. 2004, Buxton & Bailyn 2004, and §§ 2.2 and 2.3 in this work for more details).

Here we report on the *RXTE* observations during outburst decay and combine the results with the optical, infrared, and radio information to understand jet formation and its effects on the spectral and temporal properties of 4U 1543–47.

## 2. OBSERVATIONS AND ANALYSIS

### 2.1. *RXTE* Observations

We triggered our monitoring program (P70124, PI: J. A. T.) with *RXTE* after the source’s ASM count rate dropped below  $15 \text{ counts s}^{-1}$ , and the first observation took place on MJD 52,478.7. The source was already in transition from the TD to the LH state, showing broadband variability and QPOs (Kalemci et al. 2002). While the nearly daily 1–3 ks monitoring from program P70124 was going on, we triggered P70128 (PI: E. K.),

<sup>9</sup> Only recently, the reflection from the disk has been incorporated into the synchrotron jet model by Markoff & Nowak (2004). See also K rding & Falcke (2004) for a recent work on timing properties from this model.

TABLE 1  
SPECTRAL PARAMETERS

Obs. <sup>a</sup>	MJD	$\Gamma$	$T_{\text{in}}$ (keV)	FLUX ( $10^{-10}$ ergs cm <sup>-2</sup> s <sup>-1</sup> )		NOTES
				Power-Law	DBB	
Thermal-dominant State						
1A.....	52,464.42	2.32 ± 0.09	0.70 ± 0.01	10.19 ± 0.97	53.92 ± 0.47	
2A.....	52,466.32	2.39 ± 0.07	0.67 ± 0.01	11.96 ± 0.91	38.20 ± 0.43	
3A.....	52,468.64	2.10 ± 0.11	0.65 ± 0.01	5.06 ± 0.68	29.44 ± 0.28	
4A.....	52,470.28	2.32 ± 0.04	0.62 ± 0.01	4.99 ± 0.59	21.72 ± 0.24	
5A.....	52,472.61	2.49 ± 0.15	0.57 ± 0.01	4.69 ± 0.50	12.84 ± 0.14	
6A.....	52,473.19	2.57 ± 0.03	0.54 ± 0.01	7.69 ± 0.58	10.62 ± 0.14	
7A.....	52,473.25	2.51 ± 0.04	0.54 ± 0.01	6.36 ± 0.52	10.99 ± 0.16	
Intermediate State						
8A.....	52,474.17	2.54 ± 0.03	0.53 ± 0.01	10.38 ± 0.29	7.781 ± 0.103	Variability, state transition
9A.....	52,477.27	2.43 ± 0.01	0.47 ± 0.01	12.78 ± 0.27	2.783 ± 0.074	QPO
10B.....	52,478.68	2.43 ± 0.01	0.43 ± 0.01	11.75 ± 0.32	1.676 ± 0.058	QPO
11B.....	52,479.74	2.40 ± 0.02	0.42 ± 0.02	9.26 ± 0.12	1.324 ± 0.041	QPO
Low/Hard State						
12B.....	52,480.66	2.10 ± 0.02	0.37 ± 0.03	12.29 ± 0.10	0.365 ± 0.026	Spectral hardening, QPO
13C.....	52,481.03	2.10 ± 0.01	0.33 ± 0.03	11.44 ± 0.11	0.305 ± 0.018	High-energy cutoff, QPO
14C.a.....	52,481.16	2.02 ± 0.01	0.40 ± 0.02	11.56 ± 0.09	0.360 ± 0.028	High-energy cutoff, QPO
14C.b.....	52,481.23	2.00 ± 0.01	0.35 ± 0.03	12.01 ± 0.11	0.237 ± 0.019	High-energy cutoff, QPO
14C.c.....	52,481.29	1.96 ± 0.01	0.33 ± 0.01	12.20 ± 0.11	0.205 ± 0.012	High-energy cutoff, QPO
14C.d.....	52,481.36	1.97 ± 0.01	0.35 ± 0.02	11.97 ± 0.21	0.217 ± 0.018	High-energy cutoff (?), QPO
15B.....	52,482.91	1.78 ± 0.04	0.35	9.77 ± 0.09	0.116 ± 0.036	Smedge optical depth begins to drop; the disk temperature is fixed from this observation on
16B.....	52,483.93	1.70 ± 0.02	0.35	8.00 ± 0.09	0.056 ± 0.015	Infrared flux begins to rise
17B.....	52,484.03	1.71 ± 0.02	0.35	7.88 ± 0.16	0.031 ± 0.016	
18B.....	52,485.74	1.65 ± 0.04	0.35	4.49 ± 0.06	0.024 ± 0.016	
19B.....	52,486.80	1.64 ± 0.04	0.35	3.17 ± 0.03	0.027 ± 0.008	
20C.....	52,487.23	1.63 ± 0.01	0.35	2.62 ± 0.01	0.028 ± 0.004	MOST radio detection
21C.....	52,487.82	1.70 ± 0.02	0.35	2.17 ± 0.03	0.023 ± 0.002	
22B.....	52,488.03	1.68 ± 0.02	0.35	1.96 ± 0.03	0.020 ± 0.004	Smedge is not required; Galactic ridge emission (<5% of the total flux) is included
23B.....	52,489.20	1.70 ± 0.04	0.35	1.25 ± 0.03	0.020 ± 0.005	
24B.....	52,490.13	1.75 ± 0.02	0.35	1.05 ± 0.01	0.020 ± 0.005	Only PCA used from this observation on; ATCA radio detection
25B.....	52,491.22	1.88 ± 0.04	0.35	0.76 ± 0.02	0.014 ± 0.001	
26B.....	52,492.14	2.06 ± 0.07	0.35	0.56 ± 0.02	0.011 ± 0.002	No timing after this observation, poor statistics
27B.....	52,493.13	1.99 ± 0.06	0.35	0.47 ± 0.02	0.013 ± 0.002	Galactic ridge emission less than 15% of the total flux
28B.....	52,494.08	2.10 ± 0.05	0.35	0.47 ± 0.02	0.013 ± 0.002	
29B.....	52,496.14	2.24 ± 0.07	0.35	0.30 ± 0.01	0.010 ± 0.001	Galactic ridge emission less than 25% of the total flux
30B.....	52,497.07	2.11 ± 0.10	0.35	0.29 ± 0.01	0.010 ± 0.002	
31B.....	52,498.67	2.22 ± 0.12	0.35	0.22 ± 0.01	0.008 ± 0.002	

<sup>a</sup> “A” for observations from P70133 (PI: J. McClintock), “B” for observations from P70124 (PI: J. A. T.), and “C” for observations from P70128 (PI: E. K.). Observation 14 from P70128 is divided into four.

which provided longer exposures ( $\sim 20$  ks) to investigate the spectral and temporal properties of the source in greater detail than possible with the daily monitoring observations. For this work, we use the long observations and the first 18 observations of the monitoring program that provided high-quality spectral information. A very interesting part of the outburst, the onset of state transition, occurred before our monitoring observations had begun. To characterize this part, we use archival *RXTE* observations from P70133 (PI: J. McClintock). Table 1 shows the list of the observations used in this work.

### 2.1.1. X-Ray Spectral Analysis

For the major part of the outburst, we used both the PCA and the HEXTE instruments on *RXTE* for the spectral analysis (see Bradt et al. 1993 for instrument descriptions). For the PCA, the

3–25 keV band was used, and the response matrix and the background model were created using the standard FTOOLS (version 5.3) programs. We added 0.8% up to 7 keV and 0.4% above 7 keV as systematic errors based on fits to Crab observations close to ours (for the details of how we estimate systematic uncertainties, see Tomsick et al. 2001). We used all available PCUs for each observation, choosing the combination that would provide the maximum number of counts.

The 15–200 keV band was used for the HEXTE data. We used the response created by FTOOLS and applied the necessary dead-time correction (Rothschild et al. 1998). The HEXTE background subtraction is performed by alternating between observations of source and background fields. The relative normalization between the PCA and HEXTE is kept free. The HEXTE data were included in the spectral analysis until MJD 52,489.

After this date, the statistical quality of the HEXTE data was poor and they were not included in the analysis. We are presenting the first analysis of the HEXTE data for this source.

For all the observations, our first spectral model consisted of absorption (model “phabs” in XSPEC), a smeared edge (“smedge” in XSPEC; Ebisawa et al. 1994), a multicolor disk-blackbody (“diskbb” in XSPEC; Makishima et al. 1986), a power law (“pegpower” in XSPEC), and a narrow Gaussian to model the iron line. This model has been commonly used for the spectral analysis of GBHs in the LH state (Tomsick & Kaaret 2000; Sobczak et al. 2000). A difference between our analysis and that of Park et al. (2004) is the modeling of the iron line. For most of our observations, the statistical quality of the data is not sufficient for reliable iron-line studies, and including a narrow line instead of a broadened Laor-model iron line (Laor 1991) yielded acceptable fits. For consistency and simplicity, we left the iron line narrow, and we did not deduce any physical results from the iron-line fits. The hydrogen column density was fixed to  $4 \times 10^{21} \text{ cm}^{-2}$ , as used by Park et al. (2004). The width of the smeared edge was fixed to 7 keV. Once we fitted the observations with this model, we added a high-energy cutoff (“highcut” in XSPEC) to the model and refitted. We include the high-energy cutoff in the overall model if an  $F$ -test indicates that adding this component significantly improves the fit.

At very low flux levels, the Galactic ridge emission becomes important. Although 4U 1543–47 is not very close to the plane ( $b = +5.43^\circ$ ), there was some contribution from the ridge, evident from the detection of a narrow iron line at 6.7 keV. However, even during the observations when 4U 1543–47 was at its faintest (after MJD 52,500), it was still detectable by the PCA. We obtained a scanning observation on MJD 52,547 that showed an increase in the count rate when the *RXTE* pointing position reached the position of 4U 1543–47. Therefore, we were not able to use any of our observations as background for Galactic ridge emission. Instead, we model the ridge emission using the description given by Revnivtsev (2003). We also utilized an *XMM-Newton* observation on MJD 52,504.54 that is close to our faint *RXTE* observations (Miller et al. 2004). We fitted our PCA observation close to the *XMM-Newton* observation with a model consisting of interstellar absorption, a power law to represent 4U 1543–47 with *XMM-Newton* parameters, a second power law, and a narrow Gaussian to represent the ridge emission. We fixed the second power-law index to 2.15, consistent with Revnivtsev (2003), which resulted in a  $1.2 \times 10^{-11} \text{ erg cm}^{-2} \text{ s}^{-1}$  Galactic ridge contribution in the 3–25 keV band. If the index is not fixed, it results in harder ridge emission.

### 2.1.2. X-Ray Temporal Analysis

For each observation, we computed the power density spectra (PDSs) and the cross spectra from the PCA data using IDL programs developed at the University of Tübingen (Pottschmidt 2002) for three energy bands: 3–6, 6–15, and 15–30 keV. We also computed a PDS for the combined band of 3–30 keV. Above 30 keV, the source is not significantly above the background for timing analysis. The PDS was normalized as described by Miyamoto & Kitamoto (1989) and corrected for dead-time effects according to Zhang et al. (1995), with a dead time of 10  $\mu\text{s}$  per event. Using 256 s time segments, we investigated the low-frequency QPOs and the timing properties of the continuum up to 256 Hz. We fitted all our PDSs with Lorentzians of the form

$$L_i(f) = \frac{R_i^2 \Delta_i}{2\pi[(f - f_i)^2 + (\frac{1}{2}\Delta_i)^2]}, \quad (1)$$

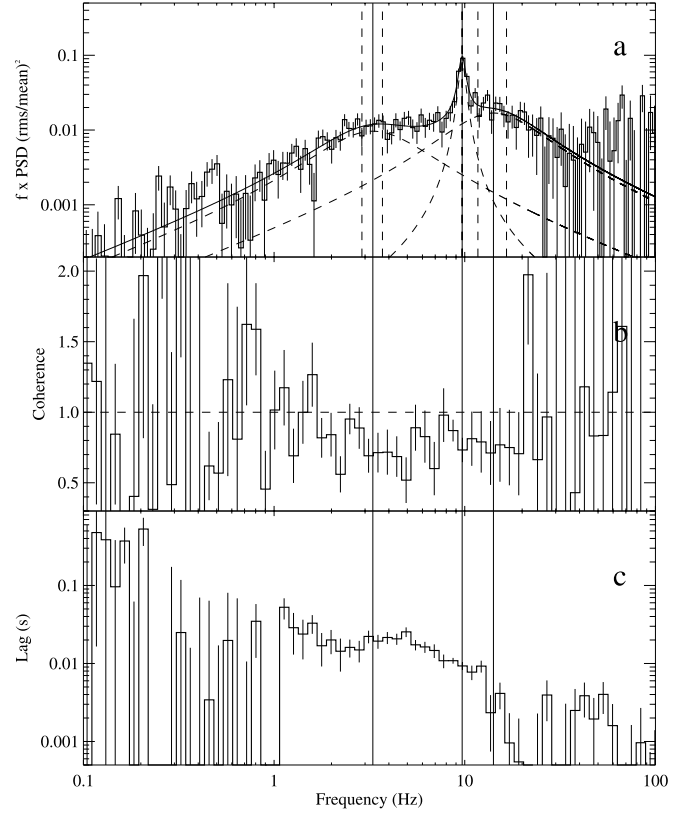


FIG. 2.—(a) Power spectrum of observation 9A in the 3–6 keV band, in the form of PDS times frequency. The Lorentzians shown with dashed curves are individual components producing the overall fit, shown with the solid curve. The solid vertical lines are peak frequencies, and the dashed lines show the  $1\sigma$  errors on the peak frequencies. (b) Coherence function for the same observation between the 3–6 keV band and the 6–15 keV band. (c) Fourier lag between the 3–6 keV and the 6–15 keV bands for the same observation.

where subscript  $i$  denotes each Lorentzian component in the fit,  $R_i$  is the rms amplitude of the Lorentzian in the frequency band from  $-\infty$  to  $+\infty$ ,  $\Delta_i$  is the full width at half-maximum, and  $f_i$  is the resonance frequency. A useful property of the Lorentzian is the “peak frequency” at which the Lorentzian contributes maximum power per logarithmic frequency interval:

$$\nu_i = f_i \left( \frac{\Delta_i^2}{4f_i^2} + 1 \right)^{1/2}. \quad (2)$$

An example power spectrum of 4U 1543–47 in the form of PDS multiplied by frequency is shown in Figure 2a. The PDS consists of broad and narrow Lorentzian fit components. In this figure the Lorentzians peak at  $\nu_i$ , demonstrating the easy identification of characteristic frequencies as peak frequencies of Lorentzian components. The peak frequencies are shown with solid vertical lines in Figure 2a. A Lorentzian with quality value  $Q_i = f_i/\Delta_i > 2$  is denoted a QPO (such as the narrow feature in the middle in Fig. 2a). The rms amplitudes are calculated over a frequency band from zero to infinity.

The cross spectrum leading to the coherence function and time lag constitutes another tool that is available as part of Fourier analysis. The coherence function is a Fourier frequency-dependent measure of the degree of linear correlation between two concurrent light curves measured simultaneously in two energy bands (Nowak et al. 1999). The Fourier time lag is a Fourier frequency-dependent measure of the time delay between two

concurrent time series (Miyamoto & Kitamoto 1989; Nowak et al. 1999). It is related to the phase of the average cross power spectrum between the soft- and hard-band light curves. We use the convention that the sign of the lag is positive when hard photons lag soft photons. Observations of hard lags in GBHs have often been interpreted as evidence of Compton upscattering in a hot electron gas (Payne 1980); however, simple Comptonization models have difficulty explaining the magnitude of the lags (Ford et al. 1999).

We calculated the coherence and lag spectrum between the 3–6 keV and 6–15 keV band light curves for all observations. Not all observations yielded meaningful coherence measurements, and the lag measurements are only meaningful when the coherence is well defined (Nowak et al. 1999). Figure 2 shows the coherence spectrum in the middle panel (Fig. 2b) and the lag spectrum in the bottom panel (Fig. 2c) for observation 9A. For observations close to the transition (such as the one in Fig. 2), meaningful (not noisy) coherence and lag values were observed between 1 and 10 Hz. To understand the trends in the amplitude of these quantities, we calculated the mean lag and the mean coherence, similar to what was done in Kalemci et al. (2003).

## 2.2. Optical and Infrared Observations

The optical/infrared (OIR) data sets were taken directly from Buxton & Bailyn (2004), and therefore we give only a short summary of how these observations were obtained. The details can be found in Buxton & Bailyn (2004). Daily *V*- and *J*-band images were taken using the YALO 1.0 m telescope from MJD 52,423. Daily *K*-band observations were initiated on MJD 52,440. The optical observations with *B*, *V*, and *I* filters were conducted between MJD 52,442.9 and MJD 52,500.8 using the 74 inch (1.9 m) telescope at Mount Stromlo Observatory. In this work, only the *J*-band light curve is shown, as the important features are most visible in the infrared. The light curves of the remaining bands can be found in Buxton & Bailyn (2004).

## 2.3. Radio Observations

The source was also observed at radio frequencies, and the details of the Molonglo Observatory Syntheses Telescope (MOST) and Giant Metrewave Radio Telescope (GMRT) observations are discussed by Park et al. (2004). Here we give a summary of these observations. The source was detected in radio several times between MJD 52,443 and MJD 52,447 by MOST and GMRT. After MJD 52,447, the source was radio-quiet until MJD 52,487. The upper limits for MOST and GMRT observations on MJD 52,480 are 3.0 and 3.2 mJy, respectively. On MJD 52,487, in the LH state, MOST detected the source at  $5.2 \pm 0.9$  mJy. The final observation by MOST, on MJD 52,496.33, did not detect the source, with an upper limit of 2.4 mJy (Park et al. 2004).

We observed 4U 1543–47 five times during 2002 June and August with the Australia Telescope Compact Array (ATCA). In each case the primary calibrator was PKS 1934–638 and the secondary calibrator was PMN J1603–4904. Observations took place at 4.80 and 8.64 GHz with a bandwidth of 128 MHz. The data were reduced in the standard way with (minimal) flagging, flux and phase calibration, and finally mapping using MIRIAD (Sault et al. 1995). A point source was fitted to the detected emission and the flux density measured. A radio source was detected twice, first on MJD 52,445 at  $3.18 \pm 0.19$  mJy (4.80 GHz) and  $2.76 \pm 0.07$  mJy (8.64 GHz), and second on MJD 52,490 at  $4.00 \pm 0.05$  mJy (4.80 GHz) and  $4.19 \pm 0.06$  mJy (8.64 GHz). On MJD 52,450, 52,451, and 52,453, during the TD state, the source was radio-quiet, with upper limits ranging between 0.2 and 3.0 mJy.

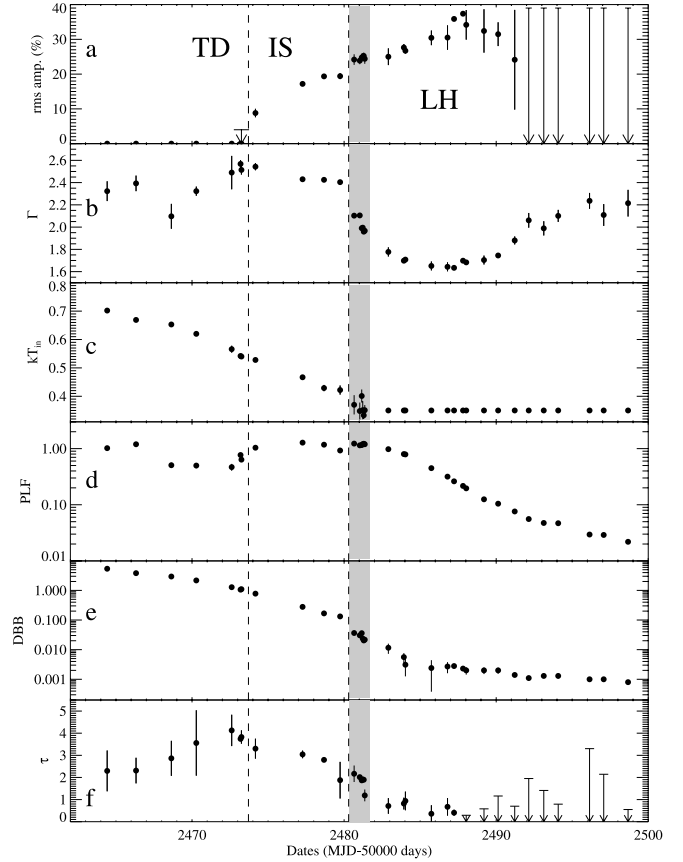


FIG. 3.—Evolution of (a) the total rms amplitude of variability in the 3–30 keV band, (b) the photon index ( $\Gamma$ ), (c) the inner disk temperature  $kT_{\text{in}}$ , (d) the power-law flux in the 3–25 keV band in units of  $10^{-9}$  ergs  $\text{cm}^{-2}$   $\text{s}^{-1}$ , (e) the disk-blackbody flux in the 3–25 keV band in units of  $10^{-9}$  ergs  $\text{cm}^{-2}$   $\text{s}^{-1}$ , and (f) the optical depth of the smeared-edge component in the fit. Unabsorbed fluxes were used. For most of the flux measurements, the  $1\sigma$  uncertainties are smaller than the plot symbols;  $2\sigma$  upper limits are shown with arrows. The dashed lines indicate approximate times of state transitions. The gray area shows the observations during the transition to the LH state.

## 3. RESULTS

### 3.1. Evolution in the X-Ray Regime

To be able to determine the sequence of events during the decay of the outburst, we investigated the evolution of several spectral and temporal fit parameters, as well as the infrared and radio fluxes. To establish the times of state transitions, we use a plot of several parameters as a function of time (Fig. 3). The main spectral fit parameters are also tabulated in Table 1.

#### 3.1.1. States and Transitions

In Figure 3, we marked the time of the first state transition at MJD  $\sim 52,474$  (between observations 7A and 8A in Table 1), when the source showed a sharp increase in the rms amplitude of variability accompanied by a sharp increase in the power-law flux. Before this date, the spectra were dominated by the disk component (more than 80% of the total flux in the 3–25 keV band), and hence the source was in the TD state. Within a few days, the power law became the dominant component in the spectrum, and the rms amplitude of variability increased to  $\sim 18\%$ . A QPO appeared in the PDS (see Fig. 4). Note that during this time, while the rms amplitude of variability and the power-law flux were changing rapidly, the photon index remained almost constant, and the inner disk temperature ( $T_{\text{in}}$ ) and the disk-blackbody (DBB) flux decayed smoothly, consistent with the observations

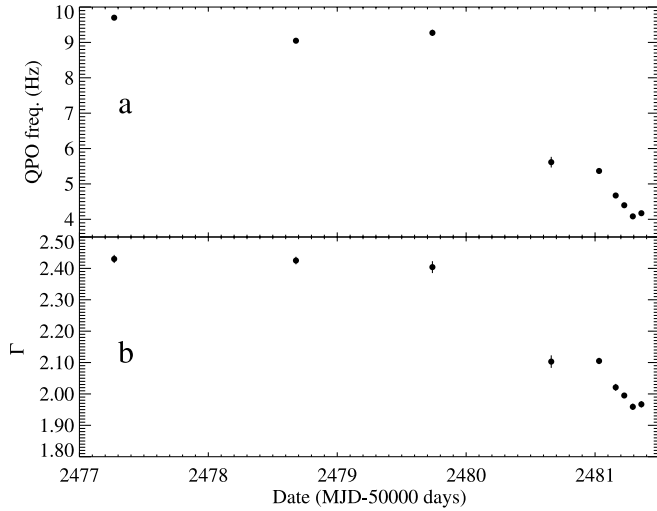


FIG. 4.—(a) QPO frequency (for the times when the QPO is observed); (b) photon index of 4U 1543–47 in the IS and during the transition to the LH state.

reported in Kalemci et al. (2004). The source was in the IS during this time, based on the softness of the photon index and the relatively comparable contributions of the hard and the soft components to the spectrum.

Around MJD 52,480 (observation 12B in Table 1), another set of sharp changes occurred; the rms amplitude of variability jumped to the  $\sim 24\%$  level, accompanied by a sharp hardening of the photon index and rapid cooling of the inner disk temperature. The power-law flux increased slightly, and the DBB flux decreased, still smoothly but more rapidly. The overall effect was total dominance of the power-law flux over the whole spectrum. After all these rapid changes (shown by the gray area in Fig. 3), the source was in the LH state. In this state, the rms amplitude of variability continued to increase before leveling off at  $\sim 35\%$ . The photon index stayed around 1.7 and then increased slightly after MJD 52,490. The power-law flux decayed smoothly. We fixed  $T_{\text{in}}$  to 0.35 keV, as the fit did not produce meaningful errors when we let  $T_{\text{in}}$  vary. The disk component was only affecting the first spectral bin in our fit. As long as the  $N_{\text{H}}$  value was fixed, the DBB component was required by the  $F$ -test in the fit, although its relative contribution to the overall flux is less than 5% (see Table 1).

The evolution of the smeared-edge component in the spectral fits is also worth mentioning (see Fig. 3f for the evolution of the optical depth). This component was required in the fit until MJD 52,488, although its effects are less and less pronounced after MJD 52,481. For observation 14C.d, the optical depth (which may be related to reflection fraction) in the “smedge” component was  $\sim 2$ . It dropped down to  $\sim 0.8$  on MJD 52,483 and stayed between 0.5 and 0.7 for the next six observations. This evolution may indicate that the reflection fraction dropped as the source went into the LH state. After MJD 52,488, the smedge component was not required in the fit, although the reduced quality of the spectra prevented us from placing strong upper limits on the optical depth of the component after MJD 52,492.

### 3.1.2. Short-Timescale Evolution

The first long observation in program P70128 was well timed, in that it was conducted when the source was in transition to the LH state, while changes were happening rapidly. In order to quantify these changes, we divided the long observation into five sections (naturally separated by occultations, with each piece

TABLE 2  
HIGH-ENERGY CUTOFF PARAMETERS

Observation	MJD	$E_{\text{cut}}$ (keV)	$E_{\text{folding}}$ (keV)
13C.....	52,481.03	$56 \pm 15$	$98 \pm 53$
14C.a.....	52,481.16	$56 \pm 10$	$79 \pm 32$
14C.b.....	52,481.23	$38 \pm 15$	$197 \pm 88$
14C.c.....	52,481.29	$45 \pm 7$	$86 \pm 28$
14C.d.....	52,481.36	$34 \pm 13$	$320^{+410}_{-130}$

having three PCUs on). Including these pieces, we show that the QPO frequency and the photon index are strongly correlated (with linear correlation coefficient of 0.995) in the IS and during the transition (see Fig. 4). Note that the last six observations are only 2–3 hours apart! A QPO frequency–photon index correlation has previously been recognized (Kalemci 2002; Vignarca et al. 2003), but we have shown for the first time that it holds on timescales as short as hours.

Another very important result that came out from the long observation is the presence of a high-energy cutoff in the HEXTE spectrum during the state transition. The cutoff is only detected significantly during the observations in which the power-law index was changing rapidly and the transition was taking place (Fig. 3, *gray area*). The cutoff and the folding energies for those observations are given in Table 2. Errors are too large to establish a pattern in the folding energy, except for observation 14C.d, for which the folding energy increased. This increase is probably a sign of a return to regular power-law shape. After this observation, the fit values for the folding energy are far beyond the HEXTE energy range, and a cutoff component is not required by the  $F$ -test. This is not the first time that the existence of a high-energy cutoff has been observed during a state transition. XTE J1550–564 during its decay in 2000 outburst showed similar behavior: the cutoff was only significant during the transition (Tomsick 2001; Rodriguez 2003).

### 3.1.3. Evolution in Temporal Parameters

The evolution of the total rms amplitude of variability and the QPO frequencies is shown in Figures 3 and 4. The QPO was detected only for the IS and during the transition to the LH state. In the LH state, the PDS can usually be characterized with two broad Lorentzians. Therefore, to understand the evolution of characteristic frequencies, we used the broad Lorentzian with the lowest peak frequency, which is present for all observations ( $\nu_1$ ; see eq. [2]). This evolution is shown in Figure 5b. In this figure we also show the evolution of the photon index (Fig. 5a), which is known to correlate with the temporal parameters that are discussed in this section. There is a good correlation between the photon index and  $\nu_1$ , something that has also been observed for other sources (Kalemci 2002; Pottschmidt et al. 2003). The decrease of characteristic frequencies in time after the transition to the LH state is also a known effect (Kalemci et al. 2004). Note that the characteristic frequency levels off as the photon index also levels off at low flux levels.

We also include the evolution of mean coherence and lags in the 1–10 Hz band in Figure 5. It was necessary to merge the light curves of the five observations in the LH state (15B–19B in Table 1) to improve statistics. In the IS, the coherence is relatively low, whereas the lags are high. As the source enters the LH state, the coherence increases and approaches unity, and the lag decreases. In the LH state, the coherence is high and the mean lag is low. These results are in agreement with the analysis

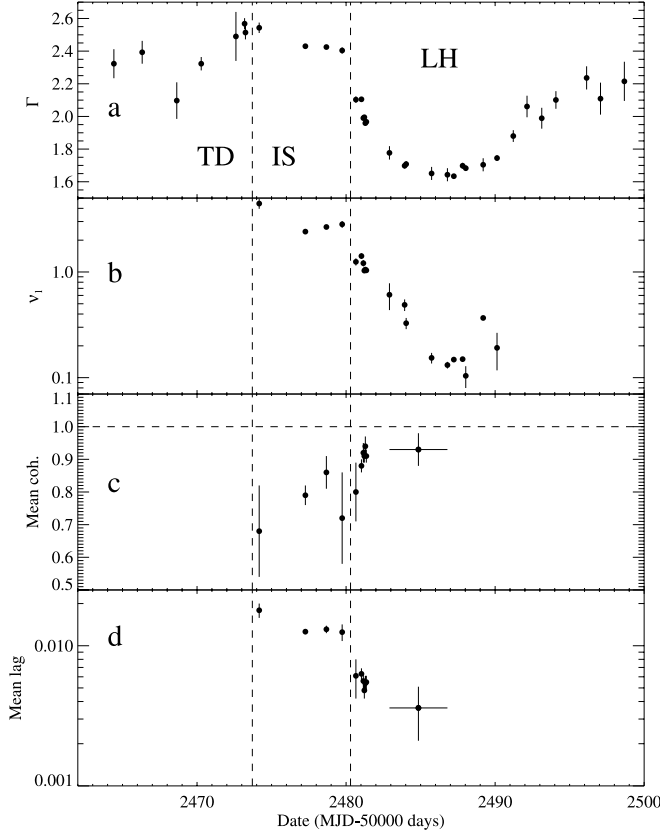


FIG. 5.—Evolution of (a) the photon index (same as Fig. 3b), (b) the lowest peak frequency ( $\nu_1$ ), (c) the mean coherence in the 1–10 Hz band between the 3–6 keV and the 6–15 keV bands, and (d) the mean lag in the 1–10 Hz band between the 3–6 keV and the 6–15 keV bands. The dashed lines represent approximate times of state transitions. Five LH-state observations were merged to obtain the last point.

of other black hole transients: high lag and low coherence during the IS, and high coherence and low (usually consistent with zero) lag in the LH state, along with a correlation between photon index and the 1–10 Hz mean lag when they are measurable (Kalemci 2002).

### 3.2. Multiwavelength Observations

Although some of the radio, optical, and infrared data from this source were presented before (Park et al. 2004; Buxton & Bailyn 2004), additional information is available when they are combined with the data from pointed *RXTE* observations. The evolution of the *J*-band fluxes, along with the radio information, is shown in Figure 6b. In Figure 6 we also show the rms amplitude of variability and the photon index (same as Figs. 3a and 3b, respectively), as well as the *HEXTE* cluster A count rate in the 16–100 keV band. The *J*-band flux decreased steadily in the TD state as the source flux was decaying. Unfortunately, there was no coverage during the first transition, making it impossible for us to determine if there was a response in the OIR emission. On the other hand, there was strong response after the transition to the LH state, such that the *J*-band flux started to increase sharply  $\sim 3$  days after the time of transition and peaked in 3 days. A two-sided Gaussian fit to the *J*-band light curve during the secondary maximum results in a peak time of MJD 52,486.3 $^{+1.5}_{-1.8}$  (Buxton & Bailyn 2004). After staying at the peak for a few days, it started to decay and reached the pre-secondary-peak levels in 7 days. As shown by Buxton & Bailyn (2004), both the optical (*B*, *V*, *I*) and the infrared light curves show this peak. It is most pro-

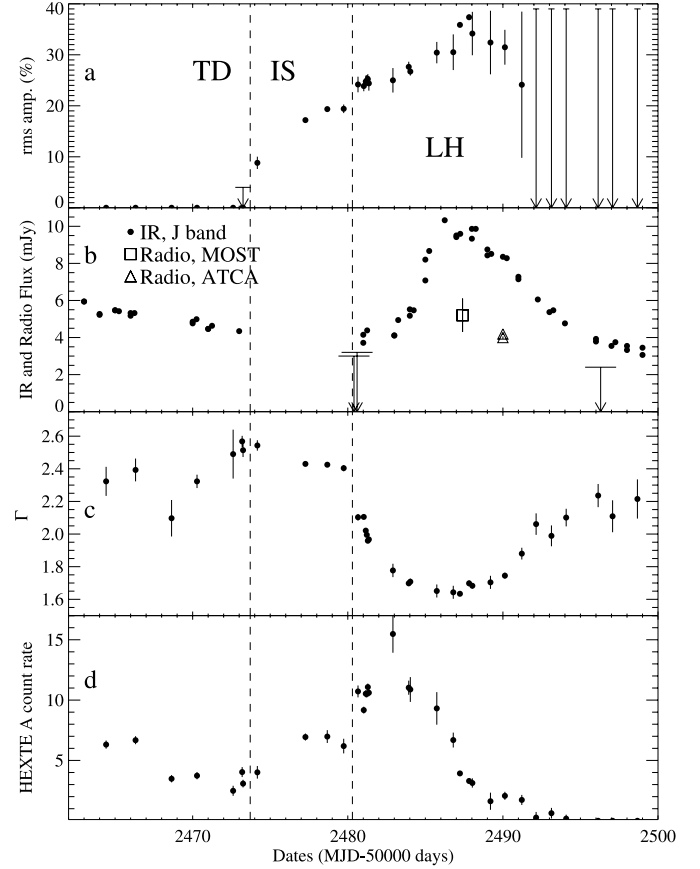


FIG. 6.—Evolution of (a) the rms amplitude of variability, (b) the *J*-band infrared fluxes from Buxton & Bailyn 2004 (circles) along with radio fluxes from our observations (triangles) and Park et al. (2004; upper limits and square), (c) the photon index, and (d) the *HEXTE* cluster A count rate in the 16–100 keV band. Note that (a) and (c) were shown before in Fig. 3. The gap in the infrared light curve during the IS is due to lack of coverage.

nounced in the *J* and the *K* bands, as the strength of emission increases with wavelength. The spectrum of the OIR points is best fitted by a power law rather than a blackbody or a DBB model (Buxton & Bailyn 2004). This strongly suggests that the origin of the OIR emission is optically thin synchrotron. From the beginning of our observations on MJD 52,464 to MJD 52,487, there was only one radio observation that resulted in no detection. The detections occurred in the LH state, during the secondary maximum. The radio emission most likely originates from an outflow, possibly a compact jet given the inverted spectrum of observation 24B (see Fig. 8 below).

While the *J*-band flux increased, the rms amplitude of variability (Fig. 6a) also increased slightly. It is not clear what happened to the rms amplitude of variability after MJD 52,492, as the count rate was too low to constrain the timing properties. The photon index (Fig. 6c), on the other hand, seemed to show an anticorrelation with the *J*-band flux. There is a  $\sim 2$  day time lag between the time at which the photon index began to harden and when the *J*-band flux began to increase. As the *J*-band flux decreased, the photon index began to soften.<sup>10</sup>

Another interesting change with respect to the changes in the OIR is the evolution of the hard flux. This is represented by the

<sup>10</sup> When not fixed in the fit, the indices of the Galactic ridge emission were consistently harder than 2.15 for the last two points. We fixed the ridge power-law index to 2.15 so that the fit resulted in a harder index for the source. The actual photon indices for these two points were probably higher.



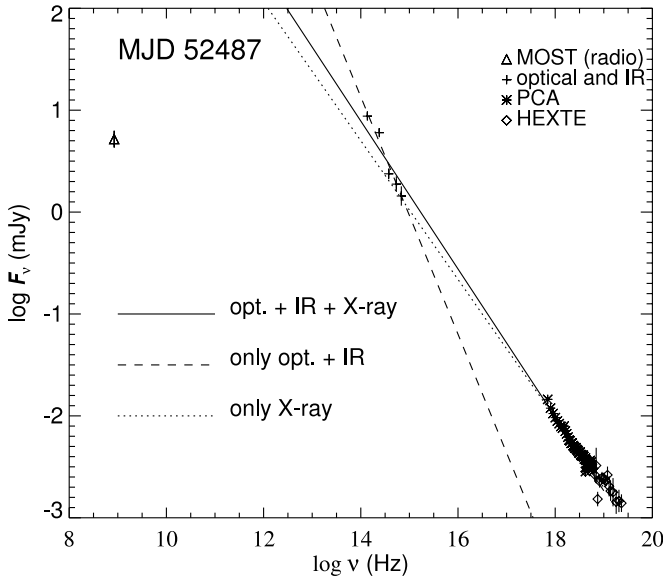


FIG. 7.—Spectral energy distribution of 4U 1543–47 at MJD 52,487. The lines represent power-law fits to different subsets of data (see Table 3).

HEXTE cluster A count rate in the 16–100 keV band in Figure 6d. First of all, there was a sharp increase in the count rate right at the transition (probably caused by sharp hardening of the X-ray spectrum). By the time the HEXTE count rate peaked, the power-law index had dipped and the  $J$ -band flux started to rise. The lag between the time that hard X-rays peaked and the OIR peaked was about 2 days.

### 3.3. Spectral Energy Distribution

We have constructed two spectral energy distributions (SEDs) close to the peak of the infrared maximum for the dates of the MOST (MJD  $\sim$ 52,487) and ATCA (MJD  $\sim$ 52,490) observations. We first corrected the OIR magnitudes for interstellar extinction using  $E(B-V) = 0.50 \pm 0.05$  (Orosz et al. 1998),  $A_V = 3.2E(B-V) = 1.60 \pm 0.16$  (Zombeck 1990),  $A_B/A_V = 1.324$ ,  $A_I/A_V = 0.482$ ,  $A_J/A_V = 0.282$ , and  $A_K/A_V = 0.112$  (Rieke & Lebofsky 1985). There were no  $B$ ,  $V$ , or  $I$  observations on MJD 52,487 (Buxton & Bailyn 2004). The source was observed in the  $B$ ,  $V$ , and  $I$  bands on MJD 52,486 and again on MJD 52,490. We used linear interpolation to estimate the peak fluxes on MJD 52,487. For each band, we fitted a line to the underlying magnitudes using the points before and after the peak to estimate the underlying flux during the secondary maximum. We converted the peak and underlying magnitudes into fluxes using the irradiation factors and description given by Zombeck (1990) and then subtracted the underlying flux from the peak flux to obtain the residual flux representing the emission from the peak only (similar to what was done in Buxton & Bailyn 2004). We used a measurement error of 0.05 mag in each band. In addition, we calculated the error due to uncertainty in extinction using the uncertainty in  $E(B-V)$ . We also obtained 0.05 and 0.08 mag uncertainties in determining the baseline fluxes for  $JK$  and  $BVI$  bands, respectively, from the fitting process. For MJD 52,487, an additional 0.05 mag uncertainty is estimated in  $B$ ,  $V$ , and  $I$  due to interpolation in finding the peak flux. All the error components were added in quadrature to estimate the total uncertainty in the measurements. The unabsorbed PCA and HEXTE fluxes for MJD 52,487 and the unabsorbed PCA fluxes for MJD 52,490 were converted into millijanskys to complete the SEDs shown in Figures 7 and 8.

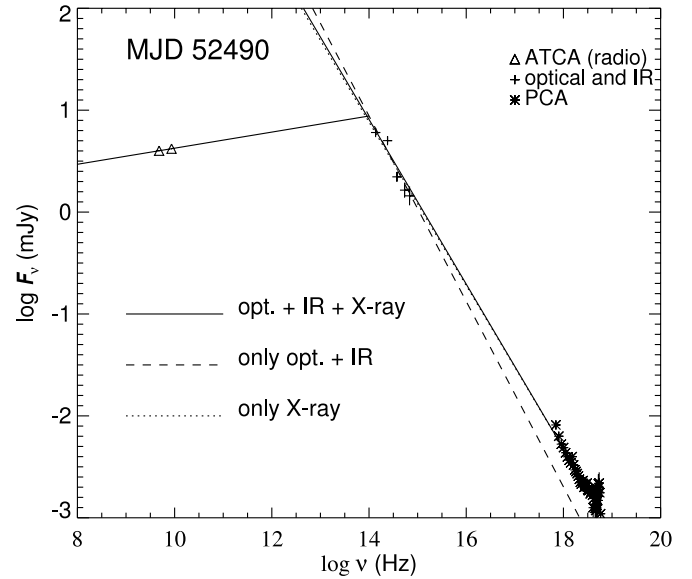


FIG. 8.—Spectral energy distribution of 4U 1543–47 at MJD 52,490. The lines passing through the optical, infrared, and X-ray points represent power-law fits to different subsets of data (see Table 3). Another line is drawn that passes through the radio points and intersects the power-law fits.

For each case, we fitted a power law to three sets of data: OIR set only, X-ray set only, and OIR and X-ray (overall) set. Figure 7 shows the SED at MJD 52,487, which includes the MOST observation, the OIR data, and the PCA and HEXTE data, as well as the power-law fits (see Table 3 for fit parameters). Statistically, the OIR points are not a continuation of the power law for the X-ray data, as the high-quality PCA and HEXTE data have a photon index of  $-1.63$  with reduced  $\chi^2$  value of 0.64 (XSPEC fit, including all other model components). The OIR points alone result in a much steeper power-law index of 2.16.

Although the OIR points again do not follow the power-law fit of the X-ray data for the SED of MJD 52,490 shown in Figure 8, the discrepancy is much less compared with the MJD 52,487 observation. The X-ray and OIR power-law indices are consistent within  $2\sigma$  uncertainty. Unlike the first case, this SED provides the break point in the spectrum, as there are two radio points. The turnover is around  $10^{14}$  Hz. This value is similar to the observed values for other sources (Corbel & Fender 2002; Homan et al. 2005).

For the  $B$ ,  $V$ , and  $I$  bands, the largest contribution to the error estimate is from the reddening. We investigated whether an underestimated error in the reddening could cause the discrepancy between the OIR slope and the X-ray slope for our SEDs.

TABLE 3  
SED POWER-LAW FIT PARAMETERS

Data Set	Photon Index	$\chi^2/\text{dof}$
MJD 52,487:		
Optical and IR only .....	$-2.16 \pm 0.10$	8.74/3
X-ray only <sup>a</sup> .....	$-1.63 \pm 0.01$	39.78/62
Optical, IR, and X-ray .....	$-1.73 \pm 0.01$	164.30/64
MJD 52,490:		
Optical and IR only .....	$-1.91 \pm 0.10$	14.66/3
X-ray only <sup>a</sup> .....	$-1.75 \pm 0.02$	47.68/43
Optical, IR, and X-ray .....	$-1.80 \pm 0.02$	80.39/42

<sup>a</sup> X-ray-only fits for both dates are from XSPEC fits, with all other model components.

For the SED on MJD 52,490, an uncertainty of 15% in  $A_V$  instead of the quoted 10% is enough to make the OIR slope and the X-ray slope be consistent within  $1\sigma$  uncertainty. However, for the SED on MJD 52,487, the uncertainty of the reddening factor must be as high as 60% to make OIR slope and X-ray slope consistent, which is highly unlikely.

### 3.4. Summary of Results

In this section we summarize our main results, which are discussed in detail in § 4.

1. The source 4U 1543–47 showed two state transitions during its decay in the 2002 outburst:

a) The first transition was from the TD state to the IS on MJD  $\sim 52,474$  and was marked by a jump in the rms amplitude of variability and power-law flux; and

b) The second transition was from the IS to the LH state and was marked by a sharp hardening of the X-ray spectrum and an increase in the rms amplitude of variability.

2. During the IS and the transition to the LH state, a QPO was detected. The resonance frequency (see eq. [1]) of the QPO shows a very strong correlation with the photon index on timescales of hours.

3. A high-energy cutoff was detected in the X-ray spectrum only during the transition to the LH state, whereas after the transition and during the LH state, the cutoff was either absent or beyond the HEXTE detection range.

4. The spectrum softened at very low flux levels in the LH state.

5. The characteristic frequencies decreased during the transition and in the LH state before they leveled off. The characteristic frequencies and the photon index show a good correlation.

6. The mean coherence was low during the IS and then increased and approached unity as the source made the transition to the LH state. The mean lag, on the other hand, was high in the IS and decreased during the transition.

7. The OIR light curves started peaking  $\sim 3$  days after the transition to the LH state. The radio detections occurred during the OIR secondary maximum.

8. The HEXTE 16–100 keV light curve increased during the transition to the LH state, while the photon index hardened. It did decay, however, while the infrared flux was rising.

9. The SEDs show that the OIR part of the spectrum can be represented by a power law. For the SED on MJD 52,487, the hard X-ray points are not a continuation of the OIR points and have a different index. For the SED on MJD 52,490, the difference is less, and the X-ray and OIR power-law indices are consistent within  $2\sigma$  uncertainty.

## 4. DISCUSSION

The multiwavelength observations of the 2002 outburst of 4U 1543–47 have provided a wealth of information on the physical processes that operate during state transitions and the LH state of GBH transients. In this section, using our observational results, previous experience from other sources, and some theoretical models, we try to place constraints on the X-ray emission geometry and the hard X-ray emission mechanism (the power-law part of the X-ray spectrum), and we try to identify the origin of the seed photons (if seed photons are required). These three properties constitute the fundamental differences between various models of X-ray emission from GBHs (Tomsick 2004).

One set of models considers a corona (which could be in the form of an advection-dominated accretion flow, or ADAF)

inside a transition radius (which can move) as the accretion geometry (see, e.g., Esin et al. 1997). In this case, the base of the jet may be the whole corona, or the base may be small compared with the overall size of the corona (Fender 2001; Markoff & Nowak 2004). We note that the jet has not been incorporated into the ADAF or “sphere plus disk” models in a self-consistent way. In the “magnetic corona” model, active, optically thin regions above the disk are responsible for the hard X-ray emission and the outflow formation (Merloni & Fabian 2002). In this model, the position of the inner edge of the accretion disk does not necessarily change significantly. For these cases in which the main hard X-ray-producing mechanism is Compton scattering, the seed photons could be produced either in the accretion disk as blackbody radiation or in the corona as synchrotron radiation (synchrotron self-Compton; Markoff & Nowak 2004). On the other hand, the main hard X-ray emission mechanism may be not Compton scattering but synchrotron radiation originating in the optically thin shock region in the jet (Falcke & Biermann 1999; Markoff et al. 2001; Markoff & Nowak 2004). A combination of emission mechanisms is also possible (see, e.g., Rodriguez et al. 2004); synchrotron radiation and Compton scattering may contribute simultaneously, and the seed photons for Compton scattering might also be a combination of synchrotron at the base of a jet or accretion disk. However, unless these mechanisms conspire to result in very similar observational properties, it may still be possible to determine the major emission mechanism and major contributor of seed photons.

The transition of 4U 1543–47 to the IS from the TD state shows characteristics that many other sources also show, namely, a strong jump in the rms amplitude of variability (from less than 4% to  $\sim 9\%$ ) accompanied by an increase in the power-law flux on a timescale of a few days. Note that during this transition, the change in the power-law photon index is smooth. Based on the similar evolution of spectral and temporal parameters of other GBH transients, in Kalemci et al. (2004) it was concluded that a threshold volume for a hot corona is required in order to observe variability. The second transition, during which the photon index and the inner disk temperature decrease very rapidly, and the multiwavelength observations in the LH state provide more insight into the hard X-ray emission mechanism for this source. Below, we describe how the sequence of observational changes may be explained by different hard X-ray emission mechanisms and geometries.

### 4.1. Compton Scattering: Recessing Accretion Disk

In the IS, the inner edge of the disk is close to the black hole, the high reflection fraction indicates that the disk and the corona have some overlap, and there is strong cooling of coronal electrons by the accretion disk seed photons. The electron distribution is most likely not Maxwellian (Coppi 1999), as no cutoff is detected in the HEXTE spectrum. It is possible that an outflow may already be present in this state that provides an “elongated” and variable corona structure at its base, which could explain large lags and small coherence values, as well as the nonthermal nature of the electron population (Pottschmidt et al. 2000; Kalemci et al. 2003).

At some critical combination of physical parameters (the mass accretion rate has been shown not to be the only parameter determining when the transition occurs; Homan et al. 2001; Kalemci et al. 2004), the inner parts of the disk evaporate rapidly into a hot corona and the transition radius moves outward. During this process, the optical thickness of the corona increases and thermal electrons dominate the system, causing a harder spectrum with a cutoff in the HEXTE band. As the disk moves outward, the hardening of the spectrum continues

because of a lower level of cooling by the disk (the cutoff becomes undetectable), and the disk temperature decreases as the hotter inner parts of the disk evaporate. Recession of the disk could also explain the evolution of the QPO frequency and  $\nu_1$  if they are related to some dynamical timescale of the inner disk. This model may further explain the correlation between the photon index and the QPO if the hardening is a direct result of less cooling due to an increasing inner disk radius, to which the QPO frequency is linked. Similar arguments have been put forward to explain the well-established correlation between photon index and reflection fraction in GBHs and active galactic nuclei (Zdziarski et al. 2002 and references therein). The relation between the photon index and the QPO frequency could also be due to increasing optical depth of the corona as it expands (Titarchuk & Fiorito 2004).

The detection of an inverted radio spectrum, and also the infrared peak, indicates that a compact jet is present deep in the LH state. The high coherence and low lag values, and the indication of a low reflection fraction, may point to the size of the jet now being small compared with the transition radius. According to Meier et al. (2001), the production region for an MHD-driven compact jet is  $(7-8)R_g$  for a Schwarzschild hole, and even smaller for a Kerr hole. A decrease by more than 1 order of magnitude in characteristic frequency between the IS and the deep LH state may also indicate that the transition radius is away from the jet production region. The detection of the QPO and the photon index–QPO frequency correlation point to an accretion disk as the major source of seed photons in the IS and during the transition. Also, once the spectrum reaches its hardest point, on MJD  $\sim 52,483$ , the HEXTE count rate starts to decrease, in parallel with the decrease in the DBB flux, again indicating that the major source of seed photons is the accretion disk. However, the source of seed photons deep in the LH state is unclear, and synchrotron self-Compton may be contributing to the hard X-ray emission after MJD  $\sim 52,487$ . The spectral softening at the end of the outburst may be due to a decrease of the optical thickness of the Comptonizing medium as the mass accretion rate decreases, and the energetic electrons either advectively accrete onto the black hole or leave the vicinity of the black hole in the form of an outflow (Esin et al. 1997). We note that this type of softening is observed in many sources (Tomsick et al. 2001; Kalemci 2002).

#### 4.2. Compton Scattering: Stable Inner Disk (Magnetic Flares)

The fits to the PCA spectrum, even at very low flux levels, require a disk component to be able to fit the first bin. However, we cannot reliably constrain disk parameters after MJD 52,485 with PCA observations when only one bin is affected. The *XMM-Newton* observation that took place on MJD 52,504.5 indicates that a disk component is required in the fit at the  $\sim 3\sigma$  level with a temperature of 0.19 keV. After converting the normalization of the DBB fit to an inner disk radius, Miller et al. (2004) claimed that the disk may still be very close to the last stable orbit. If the disk is not moving, as in the magnetic-flares model, the explanation of the spectral evolution is different from the case of a moving disk. In the stable-disk case, after the transition to the IS the active regions increase in number as compared with before the transition, and the observed variability is due to short-lived flares in the active regions (Merloni & Fabian 2001). A non-Maxwellian distribution of electrons in the corona is again required in the IS. During the transition to the LH state, a larger and larger portion of the accretion energy is used to buoy the magnetic flux tubes and to heat the corona. This results in cooling of the disk and a hardening photon index. At lower mass accretion rates, the accretion energy might be channeled into launching and sus-

taining the jet rather than heating the electrons, which may explain the softening at the end of the outburst (Merloni & Fabian 2002). The decrease in the reflection fraction could be explained if the surface of the disk becomes ionized, which would wash away the features (Nayakshin & Dove 2001). However, a recent study has shown that the magnetic-flares model cannot explain the high-energy emission of Cygnus X-1, even with the ionization effect (Barrio et al. 2003). It is also not clear what determines the QPO frequency, what causes the temporal evolution, why the characteristic frequencies decrease in time, or what causes the QPO frequency–photon index correlation.

#### 4.3. Direct Synchrotron Radiation

It is hard to explain the sequence of events in this source if the main hard X-ray emission mechanism is direct synchrotron from a shock region (first acceleration zone) in a jet for most of the outburst decay. The origin of the OIR peak emission is probably synchrotron from a shock region in the jet (where the hard X-rays would also originate), as indicated by the SEDs (Buxton & Bailyn 2004). The infrared peak shows that the shock region has formed after the transition to the LH state. Even though there is no coverage in the OIR during the IS, the infrared emission between MJD 52,480 and MJD 52,483 is the continuation of the decay in infrared before the IS, and it is unlikely that another infrared peak is present in the IS. The outflow may be present after the first transition to the IS; however, the formation of the shock region did not take place before the source was in the LH state. If the above assessment is correct, the synchrotron X-ray emission from the jet region could not have been produced before the source was deep in the LH state. But it is possible that the synchrotron emission becomes the dominant X-ray emission mechanism after the formation of the shock region. The synchrotron model results in a very low reflection fraction ( $\sim 3\%$ ; Markoff & Nowak 2004). There is a sharp drop in smeared-edge optical depth just before the infrared flux begins to rise. It is also intriguing that the QPO disappears and the structure of the power spectrum changes as the reflection decreases. However, there is also evidence against the synchrotron interpretation even after the infrared flux begins to rise. The SEDs indicate that, even without an exponential cutoff, the X-ray contribution from synchrotron is below the observed levels. More importantly, the HEXTE light curve does not follow the infrared light curve, decreasing while the infrared is still rising and the photon index is hardening between MJD 52,483 and MJD 52,487 (see Fig. 6). This is very hard to explain in the synchrotron model when the infrared and optical emission comes from the optically thin part of the SED as in 4U 1543–47 (see Figs. 7 and 8). We emphasize that the synchrotron radiation from the jet may still be contributing to the overall X-ray emission, but it cannot be the dominant emission mechanism until about MJD 52,490. It is hard to make a claim about the dominant emission mechanism after this date. Note that the discrepancy in the power-law index of the OIR points and X-ray points on MJD 52,490 is also much less than that on MJD 52,487 (see Figs. 7 and 8).

#### 4.4. Comparison with GX 339–4

When only the evolution of X-ray properties is considered, 4U 1543–47 is a very typical source, showing characteristics seen in many other GBH transients (Kalemci et al. 2004). However, this does not translate easily into generalizing the results from this work to all GBH transients, as few objects have had nearly daily simultaneous infrared and X-ray coverage such that one could compare the details of spectral evolution. GX 339–4

had such coverage during its 2002 outburst. It is also a very typical GBH transient in its spectral and timing properties. In fact, its 2002 outburst decay shows spectral and temporal characteristics in X-rays very similar to the decay of 4U 1543–47 (E. Kalemci et al., in preparation). However, in the LH state during the outburst rise, GX 339–4 showed a correlation between the X-ray flux and the OIR flux (Homan et al. 2005), whereas 4U 1543–47 shows an anticorrelation in the LH state during the decay. Although somewhat speculative, the main difference between the behavior in 4U 1543–47 and in GX 339–4 could be the origin of seed photons for Compton upscattering. For 4U 1543–47, the decay part of the HEXTE light curve seems to have two slopes: a sharp decay until MJD 52,486 and a more gradual decay after this date. This could be a sign of the major seed photon emission mechanism changing from DBB from the accretion disk to synchrotron self-Compton at the base of the jet after MJD 52,489, as the infrared and X-rays correlate after this date. Complete multiwavelength analysis (including OIR data) of other black hole transients is necessary to generalize the relation between the OIR and X-ray flux.

## 5. SUMMARY AND CONCLUSION

Using X-rays, optical/infrared, and radio observations, we have characterized the outburst decay of the Galactic black hole transient 4U 1543–47 and placed constraints on several emission models. A large, nonthermal, and radiatively inefficient outflow could explain the spectral and temporal evolution in the intermediate state. The presence of a high-energy cutoff in the X-ray spectra during the transition to the low/hard state is indicative of a thermal electron distribution. In general, our observations are consistent with a recessing accretion disk plus hot corona plus “compact” jet geometry, with the main hard X-ray emission mechanism being Compton upscattering of soft accretion disk seed photons by energetic electrons in the corona. Here we use the word “compact” to also emphasize the size of the base of the jet, which most likely is small compared with the overall size of the corona. This interpretation can reasonably explain all aspects of our observations until deep in the LH state.

Our results do not strongly rule out the possibility of the accretion disk always being close to the last stable orbit, as in the magnetic-flares model; however, the QPO frequency–photon index correlation and the decrease of characteristic frequencies with time are two results from this and other sources that need to be understood for this model (Zdziarski et al. 2003; Tomsick 2004).

Our observations disfavor synchrotron from a shock region in the jet as the major source of hard X-rays until deep in the LH state. We cannot place constraints on different emission models after MJD 52,490.

E. K. acknowledges NASA grant NAG 5-13142 and partial support from TÜBİTAK. The authors thank Sera Markoff, Jeroen Homan, and Juri Poutanen for useful discussion and comments. E. K. thanks all the scientists who contributed to the Tübingen Timing Tools. The authors thank Charles Bailyn, who (along with M. M. Buxton) provided access to the OIR data prior to publication. J. A. T. acknowledges partial support from NASA grant NAG 5-13055. M. B. gratefully acknowledges support from the National Science Foundation through grant AST 00-98421. R. E. R. acknowledges NASA grant NAS 5-30270. K. P. acknowledges support from the Deutsches Zentrum für Luft- und Raumfahrt, grant 50 OG 95030. The authors also would like to thank Jean Swank and Evan Smith for all their scheduling efforts, especially scheduling the first P70128 observation as early as possible; that observation could not have taken place at a better time. We also would like to thank Rob Fender for his help coordinating the radio observations, and Steven Tingay for conducting the ATCA observations. The Australia Telescope Compact Array is part of the Australia Telescope, which is funded by the Commonwealth of Australia for operation as a National Facility managed by CSIRO. This work has made use of data obtained through the High Energy Astrophysics Science Archive Research Center online service, provided by the NASA Goddard Space Flight Center.

## REFERENCES

- Bailyn, C. D., DePoy, D., Agostinho, R., Méndez, R., Espinoza, J., & González, D. 1999, *BAAS*, 31, 1502
- Barrio, F. E., Done, C., & Nayakshin, S. 2003, *MNRAS*, 342, 557
- Bradt, H. V., Rothschild, R. E., & Swank, J. H. 1993, *A&AS*, 97, 355
- Brockopp, C., Bandyopadhyay, R. M., & Fender, R. P. 2004, *NewA*, 9, 249
- Buxton, M. M., & Bailyn, C. D. 2004, *ApJ*, 615, 880
- Coppi, B. S. 1999, in *ASP Conf. Ser. 161, High Energy Processes in Accreting Black Holes*, ed. J. Poutanen & R. Svensson (San Francisco: ASP), 375
- Corbel, S., & Fender, R. P. 2002, *ApJ*, 573, L35
- Corbel, S., Fender, R. P., Tomsick, J. A., Tzioumis, A. K., & Tingay, S. 2004, *ApJ*, 617, 1272
- Corbel, S., Fender, R. P., Tzioumis, A. K., Nowak, M., McIntyre, V., Durouchoux, P., & Sood, R. 2000, *A&A*, 359, 251
- Corbel, S., Nowak, M. A., Fender, R. P., Tzioumis, A. K., & Markoff, S. 2003, *A&A*, 400, 1007
- Corbel, S., et al. 2001, *ApJ*, 554, 43
- Ebisawa, K., et al. 1994, *PASJ*, 46, 375
- Esin, A. A., McClintock, J. E., & Narayan, R. 1997, *ApJ*, 489, 865 (erratum 500, 523 [1998])
- Falcke, H., & Biermann, P. L. 1999, *A&A*, 342, 49
- Fender, R. 2005, in *Compact Stellar X-Ray Sources*, ed. W. H. G. Lewin & M. van der Klis (Cambridge: Cambridge Univ. Press), in press (astro-ph/0303339)
- Fender, R., et al. 1999, *ApJ*, 519, L165
- Fender, R. P. 2001, *MNRAS*, 322, 31
- Fender, R. P., & Kuulkers, E. 2001, *MNRAS*, 324, 923
- Ford, E. C., van der Klis, M., Méndez, M., van Paradijs, J., & Kaaret, P. 1999, *ApJ*, 512, L31
- Gallo, E., Fender, R. P., & Pooley, G. G. 2003, *MNRAS*, 344, 60
- Harmon, B. A., Wilson, R. B., Finger, M. H., Paciesas, W. S., Rubin, B. C., & Fishman, G. J. 1992, *IAU Circ.* 5510
- Homan, J., Buxton, M., Markoff, S., Bailyn, C. D., Nespoli, E., & Belloni, T. 2005, *ApJ*, in press (astro-ph/0501349)
- Homan, J., Wijnands, R., van der Klis, M., Belloni, T., van Paradijs, J., Klein-Wolt, M., Fender, R., & Méndez, M. 2001, *ApJS*, 132, 377
- Jain, R. K., Bailyn, C. D., Orosz, J. A., McClintock, J. E., & Remillard, R. A. 2001a, *ApJ*, 554, L181
- Jain, R. K., Bailyn, C. D., Orosz, J. A., McClintock, J. E., Sobczak, G. J., & Remillard, R. A. 2001b, *ApJ*, 546, 1086
- Kalemci, E. 2002, Ph.D. thesis, Univ. California, San Diego
- Kalemci, E., Tomsick, J., Rothschild, R., Corbel, S., Kaaret, P., & McClintock, J. 2002, *Astron. Telegram*, No. 103
- Kalemci, E., Tomsick, J. A., Rothschild, R. E., Pottschmidt, K., Corbel, S., Wijnands, R., Miller, J. M., & Kaaret, P. 2003, *ApJ*, 586, 419
- Kalemci, E., Tomsick, J. A., Rothschild, R. E., Pottschmidt, K., & Kaaret, P. 2001, *ApJ*, 563, 239
- . 2004, *ApJ*, 603, 231
- Kitamoto, S., Miyamoto, S., Tsunemi, H., Makishima, K., & Nakagawa, M. 1984, *PASJ*, 36, 799
- Körding, E., & Falcke, H. 2004, *A&A*, 414, 795
- Kong, A. K. H., Charles, P. A., Kuulkers, E., & Kitamoto, S. 2002, *MNRAS*, 329, 588
- Laor, A. 1991, *ApJ*, 376, 90
- Makishima, K., Maejima, Y., Mitsuda, K., Bradt, H. V., Remillard, R. A., Tuohy, I. R., Hoshi, R., & Nakagawa, M. 1986, *ApJ*, 308, 635
- Markoff, S., Falcke, H., & Fender, R. 2001, *A&A*, 372, L25
- Markoff, S., & Nowak, M. A. 2004, *ApJ*, 609, 972

- Matilsky, T. A., Giacconi, R., Gursky, H., Kellogg, E. M., & Tananbaum, H. D. 1972, *ApJ*, 174, L53
- McClintock, J. E., & Remillard, R. A. 2003, in *Compact Stellar X-Ray Sources*, ed. W. H. G. Lewin & M. van der Klis (Cambridge: Cambridge Univ. Press), in press (astro-ph/0306213)
- Meier, D. L., Koide, S., & Uchida, Y. 2001, *Science*, 291, 84
- Merloni, A., & Fabian, A. C. 2001, *MNRAS*, 321, 549
- . 2002, *MNRAS*, 332, 165
- Miller, J. M., Fabian, A. C., & Lewin, W. H. G. 2004, *Astron. Telegram*, No. 212
- Miller, J. M., & Remillard, R. A. 2002, *IAU Circ.* 7920
- Miyamoto, S., & Kitamoto, S. 1989, *Nature*, 342, 773
- Nayakshin, S., & Dove, J. B. 2001, *ApJ*, 560, 885
- Nowak, M. A., Vaughan, B. A., Wilms, J., Dove, J. B., & Begelman, M. C. 1999, *ApJ*, 510, 874
- Orosz, J. A., Jain, R. K., Bailyn, C. D., McClintock, J. E., & Remillard, R. A. 1998, *ApJ*, 499, 375
- Park, S. Q., et al. 2004, *ApJ*, 610, 378
- Payne, D. G. 1980, *ApJ*, 237, 951
- Pedersen, H. 1983, *Messenger*, 34, 21
- Pottschmidt, K. 2002, Ph.D. thesis, Univ. Tübingen
- Pottschmidt, K., Wilms, J., Nowak, M. A., Heindl, W. A., Smith, D. M., & Staubert, R. 2000, *A&A*, 357, L17
- Pottschmidt, K., et al. 2003, *A&A*, 407, 1039
- Revnivtsev, M. 2003, *A&A*, 410, 865
- Rieke, G. H., & Lebofsky, M. J. 1985, *ApJ*, 288, 618
- Rodriguez, J., Corbel, S., Hannikainen, D. C., Belloni, T., Paizis, A., & Vilhu, O. 2004, *ApJ*, 615, 416
- Rodriguez, J., Corbel, S., & Tomsick, J. A. 2003, *ApJ*, 595, 1032
- Rothschild, R. E., et al. 1998, *ApJ*, 496, 538
- Sault, R. J., Teuben, P. J., & Wright, M. C. H. 1995, in *ASP Conf. Ser. 77, Astronomical Data Analysis Software and Systems IV*, ed. R. A. Shaw, H. E. Payne, & J. J. E. Hayes (San Francisco: ASP), 433
- Sobczak, G. J., McClintock, J. E., Remillard, R. A., Cui, W., Levine, A. M., Morgan, E. H., Orosz, J. A., & Bailyn, C. D. 2000, *ApJ*, 544, 993
- Titarchuk, L., & Fiorito, R. 2004, *ApJ*, 612, 988
- Tomsick, J. A. 2004, in *AIP Conf. Proc. 714, X-Ray Timing 2003*, ed. P. Kaaret, F. K. Lamb, & J. H. Swank (Melville, NY: AIP), 71
- Tomsick, J. A., Corbel, S., & Kaaret, P. 2001, *ApJ*, 563, 229
- Tomsick, J. A., & Kaaret, P. 2000, *ApJ*, 537, 448
- Tomsick, J. A., Kalemci, E., Corbel, S., & Kaaret, P. 2003, *ApJ*, 592, 1100
- Tomsick, J. A., Kalemci, E., & Kaaret, P. 2004, *ApJ*, 601, 439
- Vaughan, B. A., & Nowak, M. A. 1997, *ApJ*, 474, L43
- Vignarca, F., Migliari, S., Belloni, T., Psaltis, D., & van der Klis, M. 2003, *A&A*, 397, 729
- Zdziarski, A. A., Lubiński, P., Gilfanov, M., & Revnivtsev, M. 2003, *MNRAS*, 342, 355
- Zdziarski, A. A., Poutanen, J., Paciesas, W. S., & Wen, L. 2002, *ApJ*, 578, 357
- Zhang, W., Jahoda, K., Swank, J. H., Morgan, E. H., & Giles, A. B. 1995, *ApJ*, 449, 930
- Zombeck, M. V. 1990, *Handbook of Space Astronomy and Astrophysics* (2nd ed.; Cambridge: Cambridge Univ. Press)